


Acoustophoresis around an elastic scatterer in a standing wave fieldKhemraj Gautam Kshetri  and Nitesh Nama ^{*}*Department of Mechanical & Materials Engineering, University of Nebraska-Lincoln, Lincoln, Nebraska 68588, USA*

(Received 6 March 2023; accepted 11 September 2023; published 5 October 2023)

Acoustofluidic systems often employ prefabricated acoustic scatterers that perturb the imposed acoustic field to realize the acoustophoresis of immersed microparticles. We present a numerical study to investigate the time-averaged streaming and radiation force fields around a scatterer. Based on the streaming and radiation force field, we obtain the trajectories of the immersed microparticles with varying sizes and identify a critical transition size at which the motion of immersed microparticles in the vicinity of a prefabricated scatterer shifts from being streaming dominated to radiation dominated. We consider a range of acoustic frequencies to reveal that the critical transition size decreases with increasing frequency; this result explains the choice of acoustic frequencies in previously reported experimental studies. We also examine the impact of scatterer material and fluid properties on the streaming and radiation force fields, as well as on the critical transition size. Our results demonstrate that the critical transition size decreases with an increase in acoustic contrast factor: a nondimensional quantity that depends on material properties of the scatterer and the fluid. Our results provide a pathway to realize radiation force based manipulation of small particles by increasing the acoustic contrast factor of the scatterer, lowering the kinematic viscosity of the fluid, and increasing the acoustic frequency.

DOI: [10.1103/PhysRevE.108.045102](https://doi.org/10.1103/PhysRevE.108.045102)**I. INTRODUCTION**

The motion of particles under high-frequency acoustic fields, referred to as acoustophoresis, has received renewed attention due to the advent of microfluidic lab-on-a-chip technologies [1–3]. In recent years, several microfluidic systems have been demonstrated that leverage high-frequency acoustic waves for diverse applications, including fluid mixing [4–9], droplet generation [10], particle separation [11], trapping [12–15], patterning [16–20], and focusing [11,21–23]. These systems leverage the nonlinear interaction of an externally applied high-frequency acoustic field with a viscous fluid, and the presence of an oscillating interface [5,12,24–27]. These interactions lead to the generation of a radiation force field and a streaming flow field, where the latter owes its origin to the dissipation of acoustic energy in a viscous fluid, either in the bulk fluid or within the boundary layer region near a solid. The streaming and radiation fields are, in turn, leveraged to control the acoustophoretic motion of microparticles immersed within the viscous fluid.

Recently, several acoustofluidic devices have employed prefabricated structures to focus the acoustic energy in their vicinity and enable efficient fluid and particle manipulation [5,12,13,28–40]. Here, the prefabricated structures act as acoustic scatterers that perturb the externally applied acoustic field and, consequently, alter the acoustic forces experienced by the immersed microparticles around the scatterer. From a physical perspective, both the prefabricated structures and

the freely moving immersed microparticles in the fluid scatter the incoming acoustic waves. However, in this article, we distinguish between the prefabricated structure and the microparticles immersed in its vicinity by reserving the use of the term “scatterer” to refer to the prefabricated structure. In contrast, the freely moving particles immersed in the fluid are referred to as “immersed microparticles” or “particles.”

In this work, we employ a numerical model to systematically investigate the streaming and radiation force field around a scatterer placed in a standing acoustic field. We leverage our previously validated numerical framework [41–43] and the recent advances by Baasch *et al.* [44] to investigate the acoustophoretic motion of immersed microparticles around the scatterer and elucidate the impact of the choice of acoustic frequency, scatterer material, and fluid properties on this motion. To this end, we calculate the streaming and radiation force fields around the scatterer and characterize the critical transition size at which the motion of immersed microparticles shifts from being streaming dominated to being radiation dominated. We consider a range of acoustic frequencies and different combinations of scatterer materials and surrounding fluid to reveal that a smaller critical transition size can be achieved by increasing the acoustic frequency, increasing the acoustic contrast factor of the scatterer, and decreasing the fluid’s kinematic viscosity. These results explain the previously reported experimental results concerning particle trapping (or the absence thereof) near acoustic scatterers in relation to the specific choices of acoustic frequency, scatterer material, and surrounding fluid employed in these studies [12,13]. The numerical model and the results reported in this work will provide a better understanding of acoustophoresis around a scatterer and will inform the optimal choice of design and operational parameters

^{*}Also at Nebraska Center for Integrated Biomolecular Communication, University of Nebraska-Lincoln, Lincoln, Nebraska 68588, USA; nitesh.nama@unl.edu

to achieve the desired acoustophoretic motion of immersed microparticles.

II. THEORY

A. Governing equations

1. Equations for fluid

The motion of a linear viscous compressible fluid is governed by the conservation of mass and linear momentum,

$$\frac{\partial \rho}{\partial t} + \nabla \cdot (\rho \mathbf{v}) = 0, \quad (1)$$

and

$$\rho \frac{\partial \mathbf{v}}{\partial t} + \rho (\nabla \mathbf{v}) \mathbf{v} = \nabla \cdot \boldsymbol{\sigma}, \quad (2)$$

where ρ is the mass density, \mathbf{v} is the (Eulerian) fluid velocity, and $\boldsymbol{\sigma}$ is the Cauchy stress tensor,

$$\boldsymbol{\sigma} = -p\mathbf{I} + \eta[\nabla \mathbf{v} + (\nabla \mathbf{v})^T] + \left(\eta_b - \frac{2\eta}{3}\right)(\nabla \cdot \mathbf{v})\mathbf{I}, \quad (3)$$

where \mathbf{I} is the identity tensor, p is the fluid pressure, and η and η_b are the shear and bulk viscosity, respectively. We remark that the term $(\nabla \mathbf{v}) \mathbf{v}$ is sometimes alternatively written as $(\mathbf{v} \cdot \nabla) \mathbf{v}$. However, we use the former notation to indicate that this term refers to the action of a second-order tensor, $\nabla \mathbf{v}$ on a vector \mathbf{v} . These equations are supplemented by a state relation linking the density ρ and the pressure p ,

$$p = p(\rho). \quad (4)$$

Equations (1)–(4), coupled with appropriate boundary conditions, fully determine the fluid solution. However, the high frequency of the imposed acoustic field results in a large difference between the characteristic oscillation timescale and characteristic streaming timescale; this renders a direct numerical solution of these equations as impractical. Instead, following prior works [27,41,43,45,46], we employ a perturbation approach by expanding the primary unknown fields as $[A] = [A]_0 + [A]_1 + [A]_2 + \dots$, where A represents the unknown field (pressure, density, or velocity) and the subscripts denote the order of the respective field. We assume the fluid to be quiescent in the absence of acoustic actuation (i.e., at the zeroth order). Substitution of the perturbation expansion of the unknown fields into Eqs. (1)–(4) leads to the following first-order system of equations:

$$\frac{\partial \rho_1}{\partial t} + \rho_0 (\nabla \cdot \mathbf{v}_1) = 0, \quad (5)$$

$$\rho_0 \frac{\partial \mathbf{v}_1}{\partial t} = \nabla \cdot \boldsymbol{\sigma}_1, \quad (6)$$

$$p_1 = c_0^2 \rho_1, \quad (7)$$

with

$$\boldsymbol{\sigma}_1 = -p_1 \mathbf{I} + \eta[\nabla \mathbf{v}_1 + (\nabla \mathbf{v}_1)^T] + \left(\eta_b - \frac{2\eta}{3}\right)(\nabla \cdot \mathbf{v}_1)\mathbf{I}, \quad (8)$$

where c_0 is the speed of sound in the fluid. Repeating the same procedure for the second-order terms, followed by time averaging, results in a second-order system of equations,

$$\left\langle \frac{\partial \rho_2}{\partial t} \right\rangle + \rho_0 \nabla \cdot \langle \mathbf{v}_2 \rangle = -\nabla \cdot \langle \rho_1 \mathbf{v}_1 \rangle, \quad (9)$$

$$\rho_0 \left\langle \frac{\partial \mathbf{v}_2}{\partial t} \right\rangle + \left\langle \rho_1 \frac{\partial \mathbf{v}_1}{\partial t} \right\rangle + \rho_0 \langle (\nabla \mathbf{v}_1) \mathbf{v}_1 \rangle = \nabla \cdot \boldsymbol{\sigma}_2, \quad (10)$$

with

$$\boldsymbol{\sigma}_2 = -\langle p_2 \rangle \mathbf{I} + \eta[\nabla \langle \mathbf{v}_2 \rangle + (\nabla \langle \mathbf{v}_2 \rangle)^T] + \left(\eta_b - \frac{2\eta}{3}\right)(\nabla \cdot \langle \mathbf{v}_2 \rangle)\mathbf{I}, \quad (11)$$

where $\langle A \rangle$ represents the time averaging of the quantity A over the oscillation time period T , $\langle A \rangle = \frac{1}{T} \int_T A dt$. As noted later in Sec. III C, we seek steady solutions for the second-order problem. Consequently, the second-order density ρ_2 drops out of Eq. (9) and the state relation linking ρ_2 and p_2 is not needed at the second order. We defer the discussion of the appropriate boundary conditions for the first- and second-order equations to Sec. III B.

2. Equations for solid

We model the scatterer as a linear elastic solid. The balance of linear momentum for a solid, in the absence of body forces, is given as

$$\rho_s \frac{\partial^2 \mathbf{u}}{\partial t^2} = \nabla \cdot \boldsymbol{\sigma}_s, \quad (12)$$

where ρ_s is the solid density, \mathbf{u} is the displacement vector, and $\boldsymbol{\sigma}_s$ is the Cauchy stress tensor. For a linear elastic solid, the Cauchy stress tensor can be related to strain tensor $\boldsymbol{\varepsilon}$ as

$$\boldsymbol{\sigma}_s = \lambda_s (\text{tr } \boldsymbol{\varepsilon}) \mathbf{I} + 2\mu_s \boldsymbol{\varepsilon}, \quad (13)$$

with

$$\boldsymbol{\varepsilon} = \frac{1}{2}[\nabla \mathbf{u} + (\nabla \mathbf{u})^T], \quad (14)$$

where λ_s and μ_s are Lamé parameters that can be related to the velocity of P and S waves in the solid as

$$c_P = \sqrt{\frac{\lambda_s + 2\mu_s}{\rho_s}}, \quad c_S = \sqrt{\frac{\mu_s}{\rho_s}}. \quad (15)$$

Therefore, the triplet (ρ_s, c_P, c_S) defines the relevant material properties for a linear elastic solid. These values are listed in Table I for all the material choices considered in this work.

B. Background field

The scatterer and the surrounding fluid are subjected to an incident (or background) acoustic field. Following the interaction of this field with the scatterer, the immersed microparticles in the vicinity of the scatterer experience a composite field ϕ , which is the sum of the background field (ϕ^{bg}) and the scattered field (ϕ^{sc}): $\phi = \phi^{\text{bg}} + \phi^{\text{sc}}$ [44,47,48]. We consider the background field as a one-dimensional plane standing wave along the y direction as

$$\mathbf{v}_1^{\text{bg}} = \frac{\psi_a}{2} ik(e^{i(ky+\varphi)} - e^{-i(ky+\varphi)})e^{i\omega t} \mathbf{e}_y, \quad (16)$$

TABLE I. The material parameters for the immersed microparticles and the scatterer materials considered in this work [52]. The viscous acoustic contrast factors are calculated using an acoustic frequency of 900 kHz. Viscous acoustic contrast factor $\Phi_{\text{visc}} = \frac{1}{3} \text{Re}[f_0] + \frac{1}{2} \text{Re}[f_1]$ [48]. The viscous acoustic contrast factor for a rigid solid is 0.923 and 1.432 in water and oil, respectively. Compressibility is calculated as $\kappa_p = \frac{3(1-\sigma_p)}{1+\sigma_p} \frac{1}{(\rho_p c_p^2)}$; Poisson's ratio is calculated as $\sigma_p = \frac{(\frac{c_p}{c_s})^2 - 2}{2(\frac{c_p}{c_s})^2 - 2}$ [53].

Parameters	Symbol	PS	Glass	Ti	Cu	SiC	Au	Pt	Unit
Density	ρ_p	1050	2240	4480	8930	13800	19700	21400	kg m^{-3}
Longitudinal speed of sound	c_p	2400	5100	6100	5010	6660	3240	3260	m s^{-1}
Shear speed of sound	c_s	1150	2800	3100	2270	1280 ^a	1280	1730	m s^{-1}
Viscous acoustic contrast factor in water	$\Phi_{\text{visc, water}}$	0.176	0.557	0.720	0.813	0.852	0.869	0.872	
Viscous acoustic contrast factor in oil	$\Phi_{\text{visc, Oil}}$	0.201	0.690	1.036	1.267	1.348	1.381	1.386	

^aThis value was assumed to be the same as for Au, due to the lack of available experimental data.

where ω is the angular frequency, $k = \frac{\omega}{c_0} - \alpha i$ is the wave number with $\alpha = \frac{\omega^2 \eta}{2c_0^3 \rho_0} (\frac{\eta_b}{\eta} + \frac{4}{3})$ being the attenuation coefficient, φ is the phase shift, \mathbf{e}_y is the unit vector along the y direction, and ψ_a is the velocity potential amplitude,

$$\psi_a = -\frac{P_a}{i\omega\rho_0 + (\eta_b + \frac{4}{3}\eta)k^2}, \quad (17)$$

where p_a is the pressure amplitude.

C. Acoustophoretic trajectory

To characterize the acoustophoretic motion of immersed microparticles around the scatterer in relation to the choice of acoustic frequency, scatterer material, and fluid properties, we implement a particle tracking strategy. In a typical acoustofluidic setup, the particle motion is governed by the acoustic radiation force and the drag force. In general, these forces are dictated by the fluid-structure interactions that are at play as the immersed microparticle moves through the fluid domain. However, for small spherical particles that are commonly employed in microfluidic experiments, the analysis of particle motion can be greatly simplified by considering semianalytical expressions for the radiation and drag forces. Further, we consider immersed microparticles to be suspended in a suspension dilute enough to neglect both the hydrodynamic and acoustic particle-particle interactions. Noting this, the acoustic radiation force experienced by a spherical particle of radius a that is much smaller than the acoustic wavelength λ , mass density ρ_p , and compressibility κ_p can be expressed as [48]

$$\mathbf{F}^{\text{rad}} = -\pi a^3 \left[\frac{2\kappa_0}{3} \text{Re}(f_0^* p_1^* \nabla p_1) - \rho_0 \text{Re}(f_1^* \mathbf{v}_1^* \cdot \nabla \mathbf{v}_1) \right], \quad (18)$$

where $\kappa_0 = 1/(\rho_0 c_0^2)$ is the compressibility of the fluid, A^* denotes the complex conjugate of the quantity A , and the factors f_0 and f_1 are given as [48]

$$f_0 = 1 - \frac{\kappa_p}{\kappa_0}, \quad f_1 = \frac{2(1-\gamma)(\rho_p - \rho_0)}{2\rho_p + \rho_0(1-3\gamma)}, \quad (19)$$

with

$$\gamma = -\frac{3}{2}[1 + i(1 + \tilde{\delta})\tilde{\delta}], \quad \tilde{\delta} = \frac{\delta}{a}, \quad \delta = \sqrt{\frac{2\eta}{\omega\rho_0}}, \quad (20)$$

where δ denotes the thickness of the viscous boundary layer. We remark that as noted by Baasch *et al.* [44] and Pavlic *et al.* [49], Eq. (18) does not account for the microstreaming contributions to the acoustic radiation force. This results in discrepancies from the true results when the thickness of the viscous boundary layer is larger than the radius of the immersed microparticle, $\delta/a > 1$. Accordingly, this expression should be used to obtain radiation force expression only for cases when the particle size is greater than the viscous boundary layer thickness. We remark that the current study aims to understand the general trends in the acoustophoretic motion of immersed microparticles with respect to the changes in scatterer material properties and acoustic frequency. A complete analysis of the particle trajectories for the cases where particle size is smaller than the viscous boundary layer thickness would require a numerical analysis with explicit modeling of immersed microparticles, which is beyond the scope of the current work. Nonetheless, in the current study, we have taken care in choosing the material and operation parameters to be always within the $\delta/a < 1$ regime.

In addition to the acoustic radiation force, the immersed microparticles experience drag force. When the wall effects and particle-particle interactions are negligible, the hydrodynamic drag force experienced by a spherical immersed microparticle can be expressed as $\mathbf{F}^{\text{drag}} = 6\pi\eta a(\langle \mathbf{v}_2 \rangle - \mathbf{v}_p)$, where \mathbf{v}_p is the particle velocity [27,50]. Given these forces, the particle motion can be predicted via Newton's second law. Noting that the characteristic timescale of acceleration is much smaller than the timescale characterizing the motion of immersed beads, and following prior works [27,41], we neglect the inertia of the particle to reduce the Newton's second law to a force balance between radiation and drag forces. This yields the particle velocity as

$$\mathbf{v}_p = \langle \mathbf{v}_2 \rangle + \frac{\mathbf{F}^{\text{rad}}}{6\pi\eta a}. \quad (21)$$

D. Critical transition size

To investigate the acoustophoresis near the scatterer, we consider the trajectories of immersed polystyrene particles that are commonly used in microfluidic experiments. We are interested in understanding whether the motion of an immersed microparticle with a given size is dominated by the

radiation force or streaming drag force, and the critical particle size at which this motion transitions from being streaming dominated to being radiation dominated. We begin by using Eq. (18) to rearrange Eq. (21) as

$$\mathbf{v}_p = \langle \mathbf{v}_2 \rangle + \tilde{a}^2 \mathbf{v}_{1\mu\text{m}}^{\text{rad}}, \quad (22)$$

where $\mathbf{v}_{1\mu\text{m}}^{\text{rad}}$ denotes the value of the second term on the right-hand side of Eq. (21), calculated for a reference particle of size $a_{\text{ref}} = 1 \mu\text{m}$, and $\tilde{a} = a/a_{\text{ref}}$ denotes the nondimensional radius of the immersed microparticle. In Eq. (22), the first term on the right-hand side represents the contribution of the streaming to the particle velocity, while the second term represents the contribution from the radiation force. Consequently, following Barnkob *et al.* [51], we define the critical transition size a_{crit} as the size of the immersed microparticle at which $\langle \mathbf{v}_2 \rangle = \tilde{a}_{\text{crit}}^2 \mathbf{v}_{1\mu\text{m}}^{\text{rad}}$, where $\tilde{a}_{\text{crit}} = a_{\text{crit}}/a_{\text{ref}}$ refers to the nondimensional critical transition size. We note that both $\langle \mathbf{v}_2 \rangle$ and $\mathbf{v}_{1\mu\text{m}}^{\text{rad}}$ are vector-valued fields. Therefore, the critical transition size depends on the particle location, and a single value cannot be defined for the entire domain. Nonetheless, to understand the relative dominance of the streaming and radiation forces on the motion of immersed microparticles, we define an instructive maximum critical transition size by considering the maxima of individual components of the vector-valued fields, i.e., $\tilde{a}_{\text{crit}} = \sqrt{\max(\langle \mathbf{v}_2 \rangle) / \max(\mathbf{v}_{1\mu\text{m}}^{\text{rad}})}$. Therefore, the critical transition sizes reported in this article should be viewed as being illustrative of the relative impact of streaming and radiation forces on the motion of immersed microparticles.

III. NUMERICAL MODEL

A. Computational domain

Acoustic scatterers of different shapes and materials have been employed in microfluidic experiments for fluid and particle manipulation [5,12,13,30,49,56]. In this work, we consider an illustrative cylindrical scatterer with radius $a_{\text{scat}} = 5 \mu\text{m}$, which is subjected to a background standing acoustic field. Referring to Fig. 1, the fluid domain around the scatterer is modeled as being infinite by employing a perfectly matched layer that absorbs all the outgoing waves. Further, the fluid domain thickness is chosen to be large enough so as to avoid the impact of outer boundaries on the streaming field around the scatterer. A fluid domain thickness of $200 a_{\text{scat}}$ was found to be sufficient for this purpose, which agrees well with findings reported in Pavlic *et al.* [49]. In this work, we consider various choices for the scatterer material and the surrounding fluid, with relevant material properties listed in Table I and Table II, respectively.

B. Boundary conditions

In this section, we list the boundary conditions used for solving the first- and second-order system of equations. For the first-order problem, the boundary conditions at the scatterer-fluid interface ($\Gamma^{s,f}$) are given by the continuity of velocity and traction as

$$\mathbf{v}_1 = \mathbf{v}_s, \quad \boldsymbol{\sigma}_1 \mathbf{n}_f = \boldsymbol{\sigma}_s \mathbf{n}_s, \quad \text{on} \quad \Gamma^{s,f}, \quad (23)$$

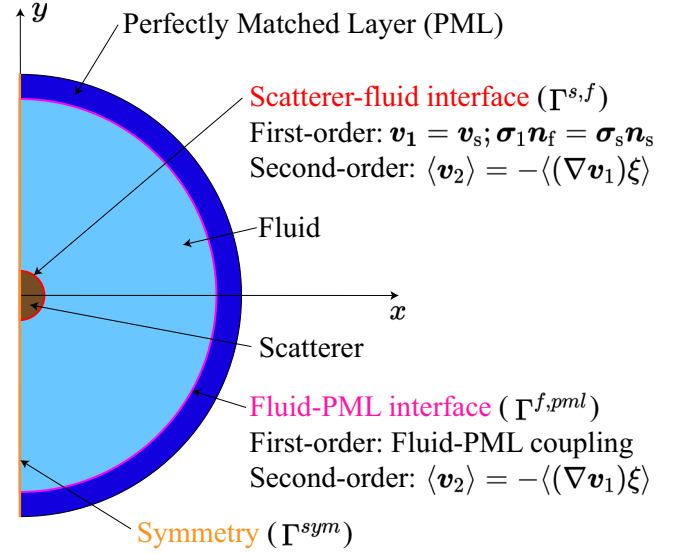


FIG. 1. Schematic illustration of the computational domain comprising an acoustic scatterer surrounded by a fluid domain, and a perfectly matched layer. The entire computational domain is subjected to a standing acoustic wave field along the y direction. The corresponding boundary conditions for the first- and second-order problems are also shown. Note that the figure is not drawn to scale.

where \mathbf{v}_s represents the velocity of the solid, and \mathbf{n}_f and \mathbf{n}_s are the unit normal vector to the scatterer-fluid interface pointing outwards from the fluid and the solid domain, respectively. Further, as shown in Fig. 1, the fluid domain is surrounded by a perfectly matched layer domain that absorbs the incoming waves and minimizes the reflections from the outer boundary of the fluid domain.

For the second-order problem, we note that owing to the linear elastic nature of the acoustic scatterer, there are no second-order contributions within the solid domain. Consequently, the second-order problem is solved only within the fluid domain. Both the scatterer-fluid interface ($\Gamma^{s,f}$) and the outer fluid boundary ($\Gamma^{f,pml}$) are assigned a Dirichlet boundary condition on the second-order velocity as

$$\langle \mathbf{v}_2 \rangle = -\langle (\nabla \mathbf{v}_1) \boldsymbol{\xi} \rangle \quad \text{on} \quad \Gamma^{s,f} \cup \Gamma^{f,pml}, \quad (24)$$

where $\boldsymbol{\xi} = \int \mathbf{v}_1 dt$ represents the first-order approximation of a lift field that is indicative of the true position of the particle at a given time [42,44,57]. We note that the second-order

TABLE II. The material properties for the fluids considered in this work [44,54,55]. The viscous boundary layer thickness is calculated using Eq. (20) for an acoustic frequency of 900 kHz.

Parameters	Symbol	Water	Oil	Unit
Density	ρ_0	998.2	922.6	kg m^{-3}
Shear viscosity	η	1.002	41.5	mPa s
Bulk viscosity	η_b	3.09	89.3	mPa s
Speed of sound	c_0	1482	1145	m s^{-1}
Viscous BL thickness	δ	0.59	3.99	μm

TABLE III. Total number of mesh elements in the computational domain for different values of δ/h .

δ/h	0.24	0.48	0.6	1.19	1.79	2.38	3.58	4.77
No. mesh elements	9802	26452	36718	111814	222690	372882	728142	1338138

problem requires the specification of an additional pressure constraint, which is enforced by specifying a constant pressure value at an arbitrary point within the fluid domain.

C. Numerical scheme

As the first-order terms in the perturbation approach are representative of the harmonic response of the fluid-solid system to the acoustic actuation, the first-order fields are taken to be harmonic in time, and we seek solutions of the form

$$\mathbf{v}_1(\mathbf{r}, t) = \tilde{\mathbf{v}}_1(\mathbf{r})e^{i\omega t}, \quad (25)$$

$$p_1(\mathbf{r}, t) = \tilde{p}_1(\mathbf{r})e^{i\omega t}, \quad (26)$$

$$\rho_1(\mathbf{r}, t) = \tilde{\rho}_1(\mathbf{r})e^{i\omega t}, \quad (27)$$

where $\tilde{\mathbf{v}}_1(\mathbf{r})$ is a complex-valued vector function of space, while $\tilde{p}_1(\mathbf{r})$ and $\tilde{\rho}_1(\mathbf{r})$ are complex-valued scalar functions of space. Further, we seek a steady solution for the second-order problem. The numerical solution is obtained via the commercial finite element software COMSOL MULTIPHYSICS 6.0 [58]. For both the first- and second-order problems, we use quadratic and linear elements for velocity and pressure, respectively.

IV. RESULTS

A. Mesh convergence analysis

To ensure that we accurately capture the first- and second-order fields near the scatterer, we perform a mesh convergence analysis. Specifically, we investigate the behavior of the radiation force field and the streaming field on a series of meshes generated by progressively decreasing the mesh element size. The different meshes are generated by varying a characteristic mesh parameter h that dictates the mesh refinement in both the fluid and solid domains. Specifically, the maximum element sizes in the fluid and solid domains are prescribed as $h_f^{\max} = 20h$ and $h_s^{\max} = h$, respectively.

We define a relative convergence function $C(g)$ for a solution g with respect to a reference solution g^{ref} [27,41],

$$C(g) = \sqrt{\frac{\int (g - g^{\text{ref}})^2 dx dy}{\int (g^{\text{ref}})^2 dx dy}}, \quad (28)$$

where the reference solution g^{ref} is obtained on the finest mesh. Here, g and g^{ref} refer to the solutions of the quantity whose convergence is being assessed. Figure 2(a) shows the results of mesh convergence analysis where the convergence function C is plotted as a function of δ/h for the four variables that govern the acoustophoretic motion, namely, F_x^{rad} , F_y^{rad} , u_2 , and v_2 , where u_2 and v_2 denote the x and y components of the second-order velocity (\mathbf{v}_2). Eight different meshes are considered with $\delta/h = 0.24, 0.48, 0.6, 1.19, 1.79, 2.38, 3.58$, and 4.77. Table III lists the corresponding number of total mesh

elements in the computational domain. We observe that all the fields reach sufficient convergence with an error of less than 0.5%, for a mesh size corresponding to $\delta/h = 2.4$. We remark that this threshold error criteria of 0.5% is chosen to achieve a good compromise between the accuracy and computational costs. To further confirm the mesh convergence of our results, Fig. 2(b) plots the critical transition size obtained on different meshes, including the finest mesh. As expected, the critical transition shows a converging trend and yields differences of less than 5 nm for meshes finer than that corresponding to $\delta/h = 2.4$. We refer the reader to the Supplemental Material [61] for further results on mesh convergence.

B. Impact of acoustic frequency

Acoustofluidic devices have employed acoustic fields with a broad range of frequencies [5,12,56]; however, the consequences of the choice of acoustic frequency on the acoustophoretic motion of immersed microparticles remain largely unknown. In this section, we assess the impact of

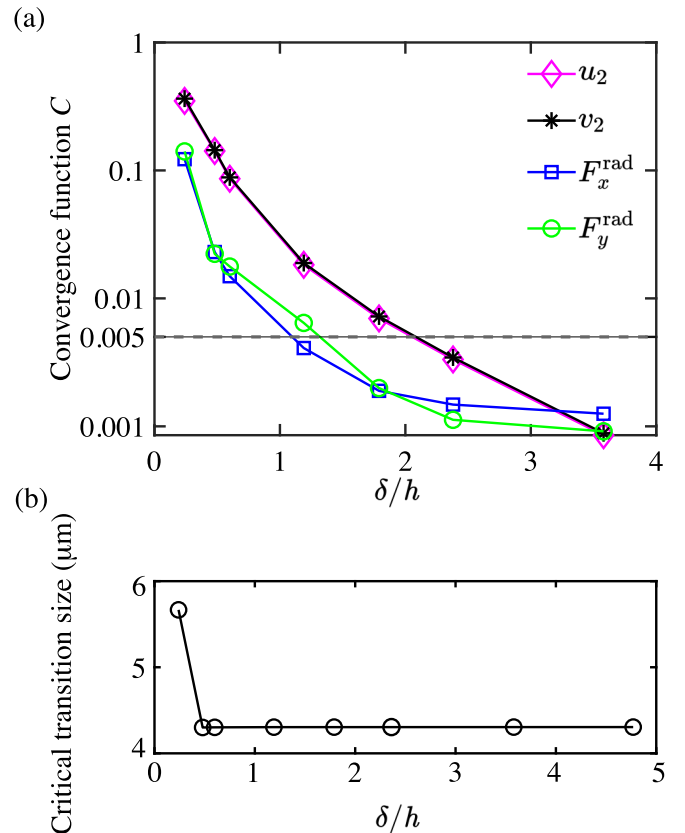


FIG. 2. Mesh convergence analysis. (a) The relative convergence parameter C , as given in Eq. (28). (b) The critical transition size for different values of the ratio of viscous boundary layer thickness and characteristic mesh size, δ/h .

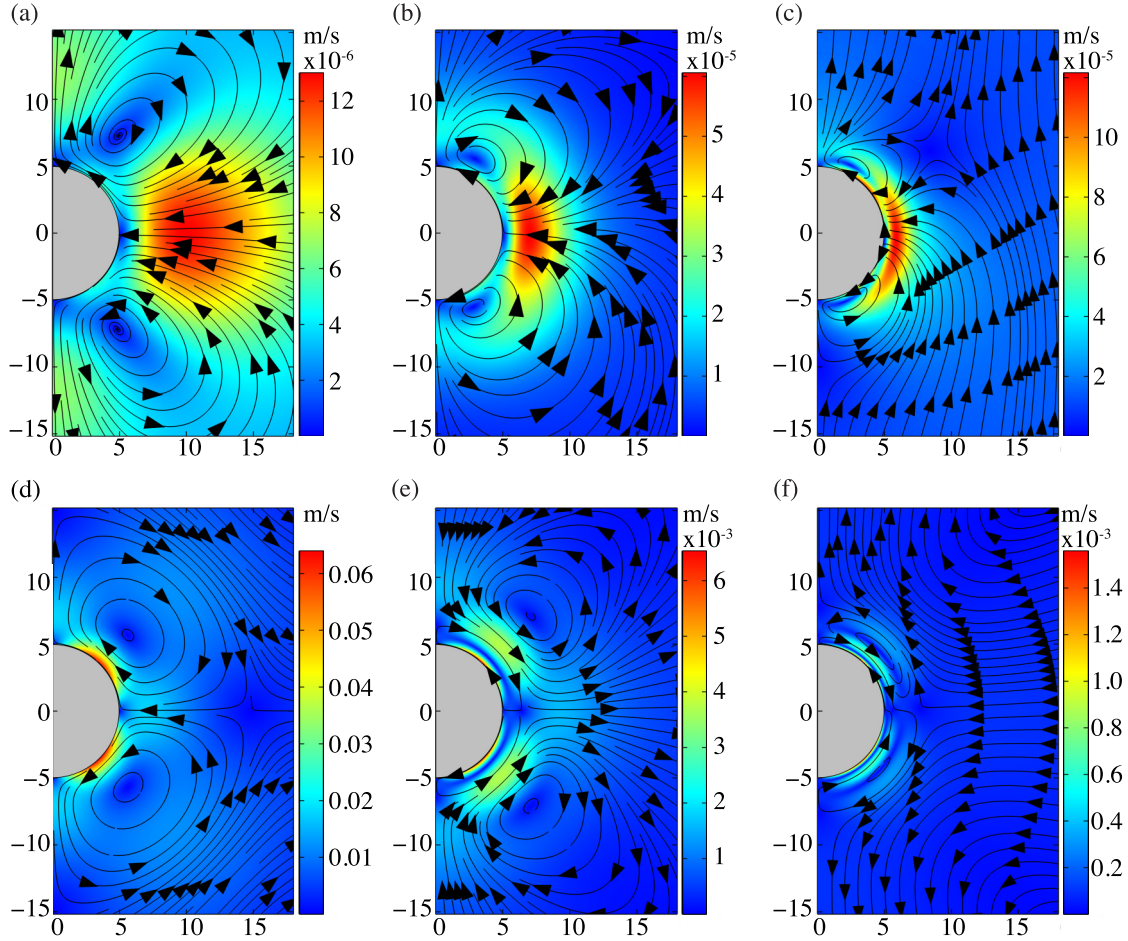


FIG. 3. Impact of frequency on the radiation-dominated velocity ($\mathbf{v}_{1\mu\text{m}}^{\text{rad}}$) and the streaming velocity ($\langle \mathbf{v}_2 \rangle$) around a $5 \mu\text{m}$ copper scatterer surrounded by water and placed between velocity node and antinode ($\varphi = \pi/4$). (a)–(c) The radiation-dominated velocity ($\mathbf{v}_{1\mu\text{m}}^{\text{rad}}$) for the acoustic frequency of (a) 5 kHz, (b) 100 kHz, and (c) 1 MHz. (d)–(f) The corresponding streaming velocity field. Color legends indicate the magnitude of the respective fields, while the numbers on the axes indicate distances in μm .

acoustic frequency on both the first- and second-order fields around a scatterer, as well as on the critical transition size defined in Sec. II D. We consider background acoustic wave fields with three different frequencies: 5 kHz, 100 kHz, and 1 MHz. In each case, we consider a $5 \mu\text{m}$ copper scatterer, placed between the velocity node and antinode of the background standing wave field ($\varphi = \pi/4$). The surrounding fluid is chosen to be water.

We begin by investigating the impact of acoustic frequency on $\mathbf{v}_{1\mu\text{m}}^{\text{rad}}$ and $\langle \mathbf{v}_2 \rangle$, where the former is indicative of the acoustic radiation force, while the latter represents the streaming solution. Figures 3(a)–3(c) show a comparison of the radiation-dominated velocity ($\mathbf{v}_{1\mu\text{m}}^{\text{rad}}$) for the three frequencies considered in our analysis, while Figs. 3(d)–3(f) show the corresponding comparison for the streaming velocity ($\langle \mathbf{v}_2 \rangle$). It can be observed that both the radiation field and the streaming field exhibit significant qualitative and quantitative changes for different frequencies. In all cases, both the radiation-dominated velocity and the streaming velocity are characterized by counter-rotating vortices. However, increasing the frequency reduces the spatial span of influence of both the radiation and streaming fields. This can be attributed to the fact that the acoustic field dissipates significantly within the

viscous boundary layer surrounding the scatterer and a higher frequency results in a thinner viscous boundary layer, leading to a reduced spatial span.

Further, for $f = 5 \text{ kHz}$, the radiation-dominated velocity is symmetric around the horizontal axis. However, this symmetry breaks down for increasing frequency: $f = 100 \text{ kHz}$ is characterized by mild asymmetry, while $f = 1 \text{ MHz}$ results in significant asymmetry around the horizontal axis. This asymmetry can be attributed to the presence of a radiation force field that arises solely due to the background standing wave field, and points towards the nearest pressure node. As the frequency increases, the contribution of the background radiation force field to the total radiation force field progressively increases. The reason behind the observed asymmetry in the radiation-dominated velocity field is further confirmed by our results that exhibit perfect symmetry for the case when the scatterer is placed at the velocity antinode (shown later in Fig. 6), where the contribution from the background radiation force field is zero.

We further note that as the acoustic frequency is increased, the maximum radiation-dominated velocity (and, hence, the maximum radiation force) increases, while the maximum streaming speed decreases. These results favor a choice of

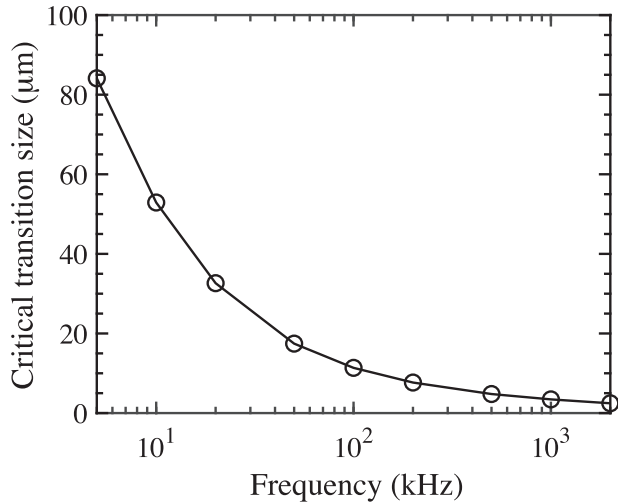


FIG. 4. Semilogarithmic plot of critical transition size as a function of acoustic frequency, obtained by considering a $5 \mu\text{m}$ copper scatterer surrounded by water and placed between velocity node and antinode ($\varphi = \pi/4$).

lower actuation frequency for applications that rely on streaming phenomena, while higher frequencies should be used for applications relying on an acoustic radiation force. This observation is in good agreement with prior experimental reports, where low acoustic frequencies (in the range of 1–100 kHz) have been used for fluid manipulation applications [5,14,30], while higher frequencies (in the range of 500–1000 kHz) have been used for particle trapping applications that rely on radiation force [12]. Nonetheless, we note that these results assess the individual impact of a change in acoustic frequency, while all other relevant parameters remain the same. A change in other parameters such as scatterer material, scatterer geometry, or the type of acoustic wave can be leveraged to realize particle trapping at low frequencies or strong streaming phenomena at high frequencies. Indeed, recent studies showed that both attraction or strong streaming are possible at high frequencies, depending on the geometry of the scatterer [59,60]. Similarly, particle trapping at frequencies below 100 kHz has also been experimentally demonstrated [62].

Next, we investigate the relationship between the acoustic frequency and the critical transition size at which the particle motion shifts from being streaming dominated to radiation dominated. We again consider a $5 \mu\text{m}$ copper scatterer in water placed between velocity node and antinode ($\varphi = \pi/4$). Figure 4 plots the critical transition size as a function of acoustic frequency. Our results reveal that the critical transition size decreases with an increase in frequency, indicating that the relative dominance of the drag force over the acoustic radiation force decreases with an increase in frequency. Our analysis also indicates that the critical transition size at frequencies below 100 kHz is in excess of $a = 10 \mu\text{m}$. We remark that given the two-dimensional (2D) nature of simulations, the results predicted from our analysis preclude the effect of microchannel confinement. Specifically, typical microfluidic channels have height of the order of 10–100 μm . For immersed microparticles with sizes similar to microfluidic channel height, the impact of microchannel confinement can be expected to

be significant, which necessitates a three-dimensional analysis. Therefore, the critical transition size prediction from our analysis for frequencies below 100 kHz should be viewed only as being indicative of the general trend that the critical transition size increases with decrease in frequency. Nonetheless, given that the typical size of immersed microparticles considered in microfluidic experiments ranges from $a = 0.1 \mu\text{m}$ to $a = 10 \mu\text{m}$, these results explain why no particle trapping was observed in our prior experimental studies on sharp-edge structures, which employed an actuation frequency of 5 kHz [30], while excellent particle trapping is observed in a similar device operated at 900 kHz [12]. These results are also in good agreement with our prior experimental report where a relatively large *C. elegans* (with typical diameter of 100 μm and length of 1 mm) could be trapped even at acoustic frequencies lower than 100 kHz, albeit with a microbubble scatterer [15].

To further understand the impact of acoustic frequency on the acoustophoretic motion of immersed microparticles, we study the motion of particles of two sizes: $a = 1 \mu\text{m}$ and $a = 5 \mu\text{m}$ for three frequencies: 5 kHz, 100 kHz, and 1 MHz. Based on the particle velocity given by Eq. (22), we expect that for streaming-dominated motion, the second term on the right-hand side is negligible compared to streaming velocity $\langle v_2 \rangle$, and therefore the particle velocity should be independent of the particle size. On the other hand, for radiation-dominated motion, the particle velocity is dominated by the second term on the right-hand side of Eq. (22); consequently, in the limit of fully radiation dominated motion, the ratio of maximum particle velocity to $v_{1\mu\text{m}}^{\text{rad}}$ should be equal to the square of the nondimensional particle size, \tilde{a}^2 . Figures 5(a)–5(c) show the acoustophoretic trajectories of $a = 1 \mu\text{m}$ particles for different frequencies, while Figs. 5(d)–5(f) shows the corresponding trajectories for $a = 5 \mu\text{m}$ particles. Referring to Figs. 5(a) and 5(d), we observe that for low frequency ($f = 5 \text{ kHz}$), both $a = 1 \mu\text{m}$ and $a = 5 \mu\text{m}$ particles follow trajectories that are both qualitatively and quantitatively similar to the streaming field, shown in Fig. 3(d), indicating purely streaming-dominated motion for both particle sizes. As the frequency is increased to $f = 100 \text{ kHz}$, the trajectories for $a = 1 \mu\text{m}$ and $a = 5 \mu\text{m}$ start to differ from each other. For $a = 1 \mu\text{m}$ particles, the trajectories are similar to the corresponding streaming field, shown in Fig. 3(e), indicating purely streaming-dominated motion. However, as the particle size is increased to $a = 5 \mu\text{m}$, the trajectories differ from the streaming field, indicating the influence of radiation force on particle trajectory.

As the frequency is further increased to $f = 1 \text{ MHz}$, the trajectories of the $a = 1 \mu\text{m}$ particles still show a qualitative similarity to the corresponding streaming velocity field [Fig. 3(f)], but quantitative differences are observed, indicating the moderate influence of radiation force. For $a = 5 \mu\text{m}$ particles, the particle trajectories are completely dissimilar to the corresponding streaming field and look qualitatively similar to the corresponding radiation-dominated velocity field, shown in Fig. 3(c). Further, the ratio of the maximum particle velocity to $v_{1\mu\text{m}}^{\text{rad}}$ is observed to be $(3.8 \times 10^{-3}) / (1.22 \times 10^{-4}) \approx 31$, which is close to the square of the nondimensional particle size, $\tilde{a}^2 = 25$; this indicates that the motion

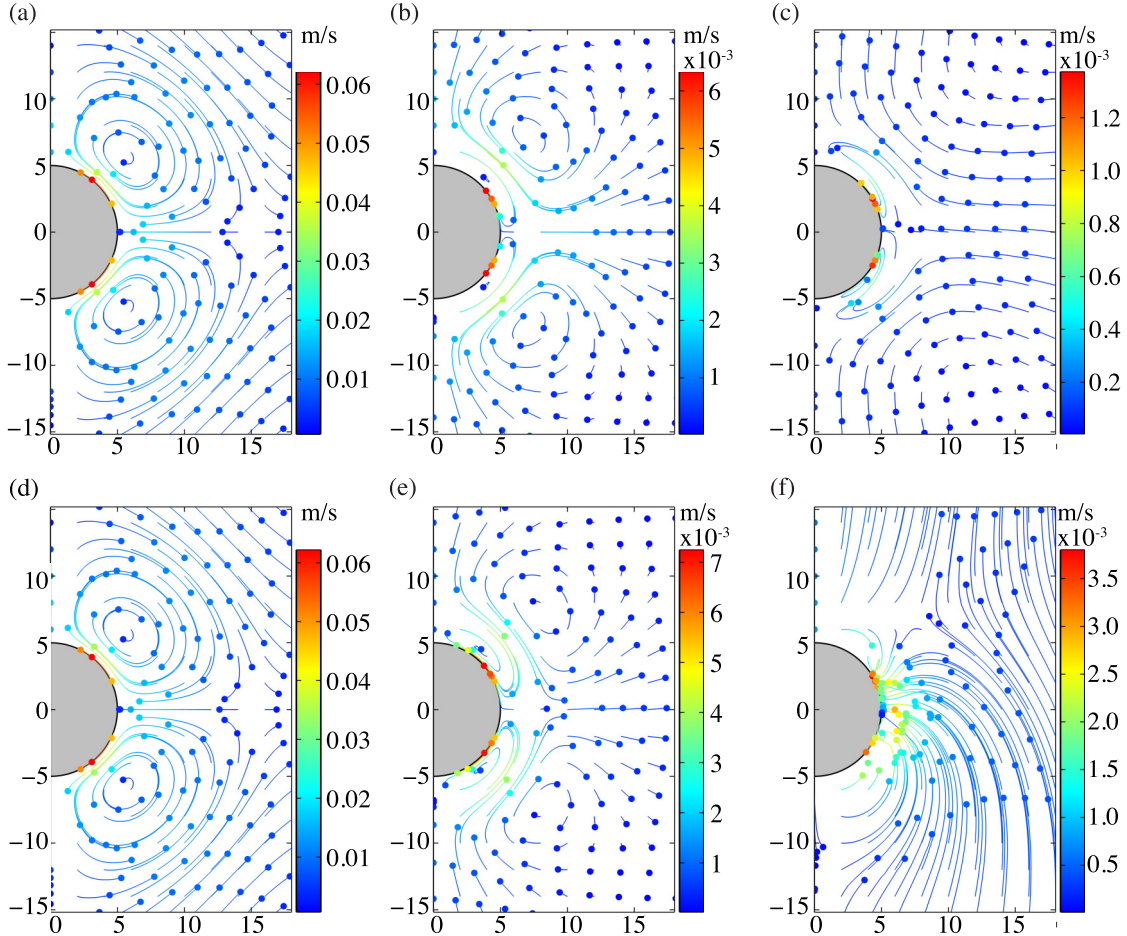


FIG. 5. Impact of acoustic frequency on trajectories of 157 evenly spaced immersed polystyrene particles around a copper scatterer. (a)–(c) The trajectories of 1 μm particles for an acoustic frequency of (a) 5 kHz, (b) 100 kHz, and (c) 1 MHz. (d)–(f) The corresponding trajectories of 5 μm particles. The immersed microparticles are traced for 0.5, 3, and 25 ms for 5 kHz, 100 kHz, and 1 MHz, respectively. The colored disks represent the final position of the immersed microparticles moving along colored lines. Color legends indicate the magnitude of the particle velocity, while the numbers on the axes indicate distances in μm .

of $a = 5 \mu\text{m}$ particles at 1 MHz is significantly dominated by the radiation force. Choosing an even bigger particle size brings this ratio closer to the expected value of \tilde{a}^2 , indicating the motion to be purely radiation dominated. Therefore, our results reveal that the motion of a given particle size (say, $a = 5 \mu\text{m}$) can be tuned to be either streaming dominated [Fig. 5(d)] or radiation dominated [Fig. 5(f)] by tuning the actuation frequency.

C. Impact of scatterer material

In this section, we focus our attention on understanding the impact of scatterer material on the acoustophoretic motion of immersed microparticles. To this end, we consider four different cases with the scatterer modeled as glass, titanium, platinum, and a perfectly rigid material. In this article, we use the term rigid material to refer to a material with compressibility limiting towards zero, and density much larger than that of the surrounding fluid ($\rho_p/\rho_0 \gg 1$). This corresponds to $f_0 = 1$ and $f_1 \approx 1 - \gamma$ for a rigid solid. In each case, the fluid is taken to be water, the acoustic frequency is chosen to be $f = 900 \text{ kHz}$, the scatterer size is $a_{\text{scat}} = 5 \mu\text{m}$, and the

scatterer is positioned at the velocity antinode of the standing wave ($\varphi = \pi/2$). Given the same choice of fluid in all cases, a change in scatterer material properties results in a change in the acoustic contrast factor, as noted in Table I.

Figure 6 plots $\mathbf{v}_{1\mu\text{m}}^{\text{rad}}$ and $\langle \mathbf{v}_2 \rangle$ for each case. It can be observed that the choice of scatterer material has a significant impact on both the radiation force field (indicated by plots of $\mathbf{v}_{1\mu\text{m}}^{\text{rad}}$) and the streaming field. Specifically, the radiation force field for nonrigid scatterers [Figs. 6(a)–6(c)] is characterized by two counter-rotating vortices. We note that these results are seemingly surprising since the acoustic radiation force field is typically understood as being a focusing force field that is responsible for the trapping of particles at the scatterer-fluid interface, while the vortical motion of immersed microparticles is typically ascribed to the streaming flow. However, as the contrast factor is increased, the center of these vortices moves closer to the scatterer-fluid interface and disappears completely in the limiting case of a rigid scatterer [Fig. 6(d)], where we observe a typical focusing force field pattern that moves the particles to the surface of the scatterer. These results are in good agreement with prior experimental observations by Leibacher *et al.* [12], where particle trapping was

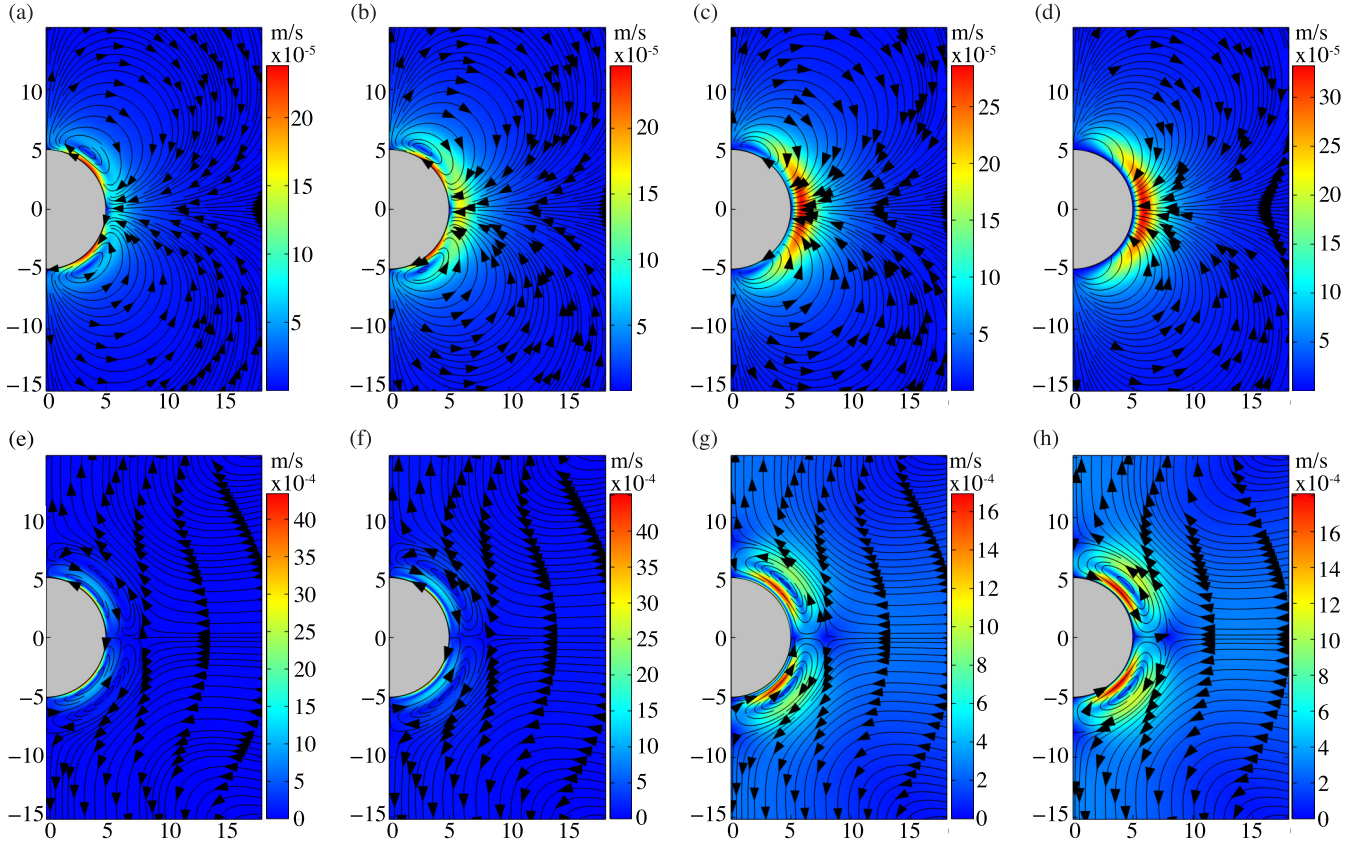


FIG. 6. Impact of scatterer material on the radiation-dominated velocity ($v_{1\mu\text{m}}^{\text{rad}}$) and the streaming velocity (v_2) around a $5\ \mu\text{m}$ scatterer surrounded by water and placed at the velocity antinode of the standing wave ($\varphi = \pi/2$) with an acoustic frequency of 900 kHz. (a)–(d) The radiation-dominated velocity ($v_{1\mu\text{m}}^{\text{rad}}$) for (a) glass, (b) titanium, (c) platinum, and (d) rigid scatterer. (e)–(h) The corresponding streaming velocity field. Color legends indicate the magnitude of the respective fields, while the numbers on the axes indicate distances in μm .

observed on scatterers made of silicon, which can be reasonably approximated as a rigid material. Our results also agree well with the theoretical analysis performed by Doinikov *et al.* [60], where a focusing radiation force field was predicted for rigid sharp edges. Overall, these results indicate that it is not only the choice of low actuation frequency ($\approx 5\ \text{kHz}$), but also the choice of polymer material (polydimethylsiloxane) with low acoustic contrast factor that contributes to the absence of particle trapping in polymer-based sharp-edge devices [5,30].

Figures 6(e)–6(h) shows the impact of scatterer material on the streaming field. It can be observed that the streaming field for nonrigid scatterer materials is characterized by three pairs of counter-rotating vortices [Figs. 6(e)–6(g)]. Further, as the acoustic contrast factor is increased, the innermost vortices move closer to the scatterer-fluid interface, and in the limiting case of a rigid scatterer [Fig. 6(h)], the streaming field is characterized by only two pairs of counter-rotating vortices.

Next, we assess the impact of scatterer material on the critical transition size. Specifically, we consider several scatterer materials with increasing viscous acoustic contrast factors relative to the surrounding fluid (water): glass ($\Phi = 0.557$), titanium ($\Phi = 0.720$), copper ($\Phi = 0.813$), silicon carbide ($\Phi = 0.852$), gold ($\Phi = 0.869$), platinum ($\Phi = 0.872$), and rigid scatterer ($\Phi = 0.923$), with the relevant material prop-

erties listed in Table I. In all cases, the acoustic frequency is chosen as $f = 900\ \text{kHz}$. Figure 7 plots the critical transition size as a function of viscous acoustic contrast factor. It can be observed that the critical transition size decreases with an

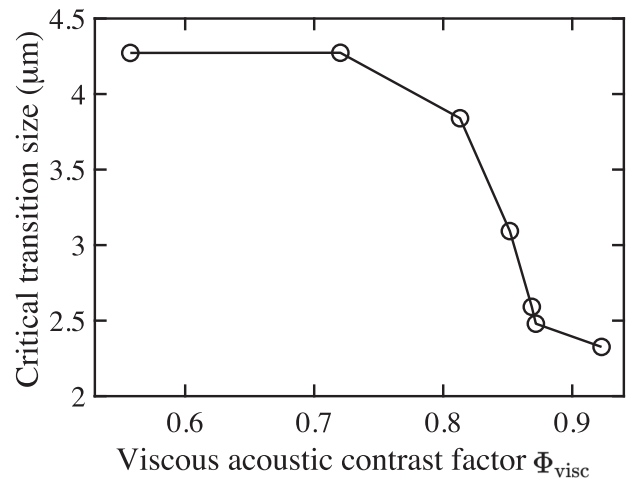


FIG. 7. Plot of critical transition size as a function of viscous acoustic contrast factor Φ_{visc} , obtained by considering different scatterer materials. In all cases, the fluid is taken to be water and the acoustic frequency is chosen as $f = 900\ \text{kHz}$.

increase in viscous acoustic contrast factor, and the minimum value of the critical transition size is reached in the limiting case of a rigid scatterer. Further, for the choices of scatterer materials and the surrounding fluid (water) considered in this analysis, our results indicate a narrow range of critical transition size, ranging from 2.33 to 4.27.

We note that in the case of immersed microparticles subjected to a purely standing wave field, the radiation force in Eq. (18) can be shown to be directly proportional to the viscous acoustic contrast factor, Φ_{visc} [48]. Consequently, for such cases, $v_{1\mu\text{m}}^{\text{rad}} \propto \Phi_{\text{visc}}$; this further implies that the critical transition size (a_{crit}) varies as $a_{\text{crit}} \propto \frac{1}{\sqrt{\Phi_{\text{visc}}}}$. In contrast, the immersed microparticles in our analysis are subjected to a complex acoustic field comprised of the background standing wave field and the scattered field due to the presence of a scatterer. In such cases, the acoustic radiation force is no longer linearly proportional to Φ_{visc} , but is rather dictated by the terms in brackets on the right-hand side of Eq. (18), which depends on the first-order pressure and velocity fields in addition to the fluid-scatterer properties.

D. Impact of fluid properties

Next, we consider the impact of the properties of the surrounding fluid on the radiation force and streaming field around the scatterer by considering two different fluids, i.e., water and oil, with the relevant properties listed in Table II. Figure 8 plots the radiation-dominated velocity ($v_{1\mu\text{m}}^{\text{rad}}$) and the streaming field (v_2) around a platinum scatterer placed at the velocity antinode of the background standing wave field with frequency $f = 900$ kHz for the two choices of the surrounding fluid. In both cases, the radiation force field is characterized by counter-rotating vortices; however, the span of these vortices is significantly larger in the case of oil. This can be attributed to the fact that the viscous boundary layer thickness in the case of oil ($3.99 \mu\text{m}$) is significantly larger than the viscous boundary layer thickness in the case of water ($0.59 \mu\text{m}$); therefore, the spatial span of viscous effects is expected to be much larger for oil.

Further, the streaming field is characterized by three pairs of counter-rotating vortices for water as the surrounding fluid, while only two pairs of counter-rotating vortices are observed when the surrounding fluid is taken as oil. This observation can be understood by noting that the viscous acoustic contrast factor for platinum-water and platinum-oil is 0.872 and 1.381, respectively, and, as observed from Fig. 6, the innermost pair of streaming vortices progressively diminishes as the acoustic contrast factor is increased.

Similar to Fig. 7, we repeat our analysis to investigate the critical transition size as a function of scatterer material, but with the surrounding fluid as oil instead of water. Again, we consider several scatterer materials with varying viscous acoustic contrast factors relative to the surrounding fluid: glass ($\Phi = 0.690$), titanium ($\Phi = 1.036$), copper ($\Phi = 1.267$), silicon carbide ($\Phi = 1.348$), gold ($\Phi = 1.381$), platinum ($\Phi = 1.386$), and rigid scatterer ($\Phi = 1.432$). Figure 9 plots the critical transition size as a function of viscous acoustic contrast factor. Comparing Fig. 9 to Fig. 7, a similar qualitative trend can be observed where the critical transition size decreases with an increase in viscous acoustic contrast

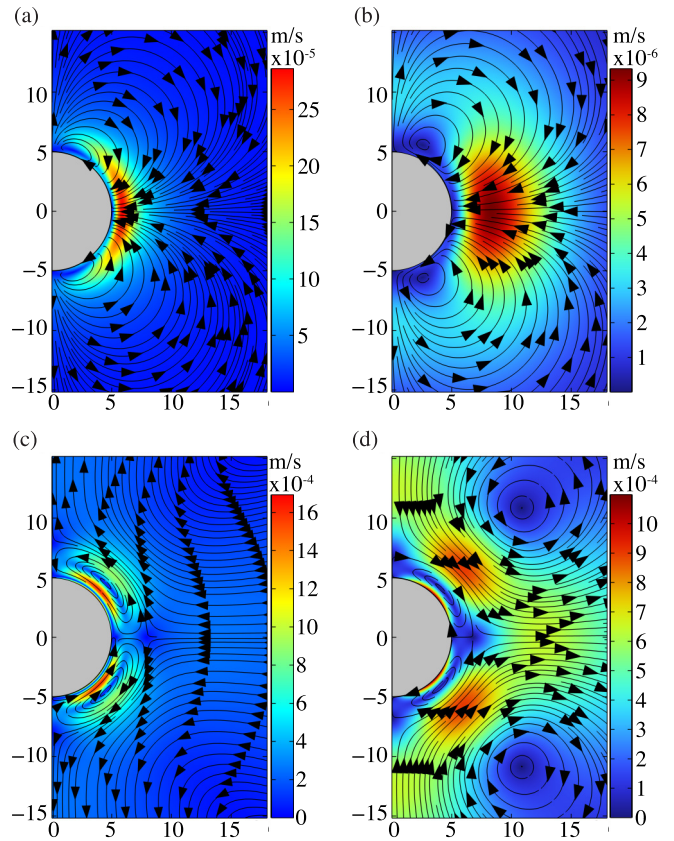


FIG. 8. Impact of fluid properties on the radiation-dominated velocity ($v_{1\mu\text{m}}^{\text{rad}}$) and the streaming velocity (v_2) around a $5 \mu\text{m}$ platinum scatterer placed at the velocity antinode of the standing wave with an acoustic frequency of 900 kHz. (a),(b) The radiation-dominated velocity ($v_{1\mu\text{m}}^{\text{rad}}$) for (a) water and (b) oil. (c),(d) The corresponding streaming velocity field. Color legends indicate the magnitude of the respective fields, while the numbers on the axes indicate distances in μm .

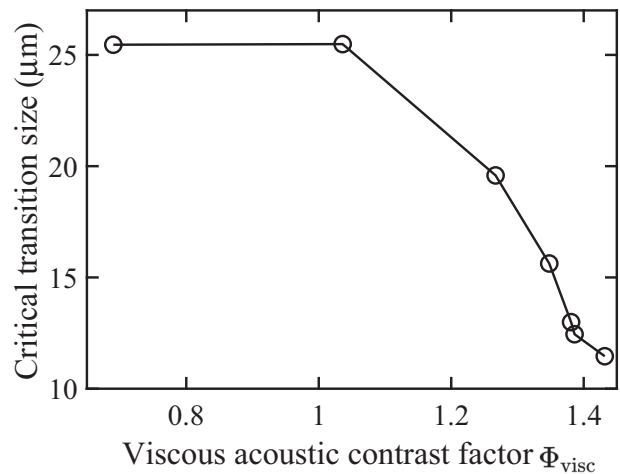


FIG. 9. Plot of critical transition size as a function of viscous acoustic contrast factor Φ_{visc} , obtained by considering different scatterer materials. In all cases, the fluid is taken to be oil and the acoustic frequency is chosen as $f = 900$ kHz.

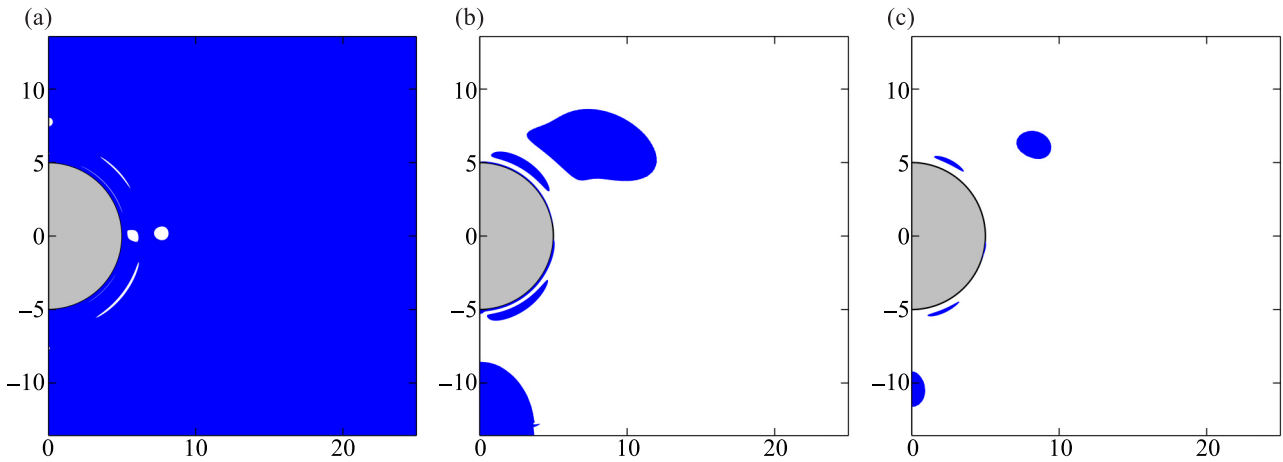


FIG. 10. Spatial analysis of critical transition size. (a)–(c) The spatial dominance of the streaming (v_2) and radiation force ($v_{1\mu\text{m}}^{\text{rad}}$) field on the motion of immersed particles of size 1, 3, and 5 μm , respectively. The blue space represents the streaming-dominated field, while the white represents the radiation-force-dominated field. The numbers on the axes indicate distances in μm .

factor, and the minimum value of the critical transition size is reached in the limiting case of a rigid scatterer. However, we note that the range of both the critical transition size and the acoustic contrast factor for the considered materials is much larger in the case of oil. Further, if we compare the glass-water combination (second point from the left in Fig. 7) with the titanium-oil combination (first point from the left in Fig. 9), we observe that the critical transition size for these two cases is significantly different, despite having a similar value of contrast factor. This difference in critical transition size can be attributed to the difference in the kinematic viscosity of water and oil ($\nu_{\text{water}} = 1 \times 10^{-6} \text{m}^2/\text{s}$ vs $\nu_{\text{oil}} = 45 \times 10^{-6} \text{m}^2/\text{s}$). Specifically, for immersed microparticles subjected to one-dimensional standing wave fields, the theoretical analysis reported by Barnkob *et al.* [51] predicts that the critical transition size varies as $a_{\text{crit}} \propto \sqrt{\nu}$, for a given acoustic frequency and contrast factor. In contrast to the analysis by Barnkob *et al.* [51], the immersed microparticles in our case are subjected to an acoustic field characterized by the combination of a background standing acoustic field and the scattered field; nonetheless, we observe a similar trend in critical transition size, with the critical transition size in oil being approximately $\sqrt{\frac{\nu_{\text{oil}}}{\nu_{\text{water}}}} = 6.7$ times that in water. Accordingly, a larger range of critical transition size can be achieved in oil compared to that in water for a given operational frequency. Further, these results demonstrate that a smaller critical transition can be realized in scatterer-based acoustofluidic systems by reducing the kinematic viscosity of the surrounding fluid. Combined with the results reported in Secs. IV B and IV C, our results reveal a potential pathway to realize the manipulation of small particles by tuning the acoustic frequency and the scatterer-fluid material properties.

E. Spatial analysis of critical transition size

Next, we investigate the spatial range of the effective dominance of streaming field and radiation force field on the motion of immersed particles in the vicinity of a scatterer. We consider a copper scatterer of 5 μm placed in between

the velocity node and antinode of a standing wave field with an acoustic frequency of 1 MHz. For this configuration, we consider the relative dominance of the streaming and radiation force contributions to the particle velocity by considering three sizes of immersed microparticles: 1, 3, and 5 μm . As indicated in Eq. (22), the particle velocity can be viewed as the sum of a streaming contribution and a radiation force contribution. Noting this, Figs. 10(a)–10(c) plot the areas (in blue) where the streaming contribution to the particle velocity is larger than the radiation force contribution. Conversely, the areas where the radiation force contribution is larger than the streaming contribution are shown in white. As expected, for small microparticles (1 μm), the particle velocity in most of the regions is dominated by the streaming contributions. However, as the particle size increases to 3 μm , the spatial extent of the streaming-dominated areas decreases. Further increase in particle size to 5 μm results in the almost complete disappearance of streaming-dominated regions, indicating that the motion of particles of 5 μm is dominated by a radiation force in most regions of the domain. These results for spatial analysis of the critical transition size are in good agreement with the critical transition size predicted based on maximum values, which indicated a critical transition size of 3.44 μm for this case.

F. Directional dependence of the relative dominance of streaming and radiation force contributions

Lastly, we investigate the directional dependence of the relative dominance of the streaming and radiation force fields on the motion of immersed microparticles. We consider the same operating parameters as the previous section. Figure 11 plots the relative velocity magnitude due to streaming and radiation force along different radial directions (i.e., along radially drawn line segments with different angles relative to the x axis). First, we consider variations of the streaming and radiation force contributions along a radial line passing through the center of the scatterer and drawn along the x axis (i.e., at 0° relative to the x axis). In this case, the immersed

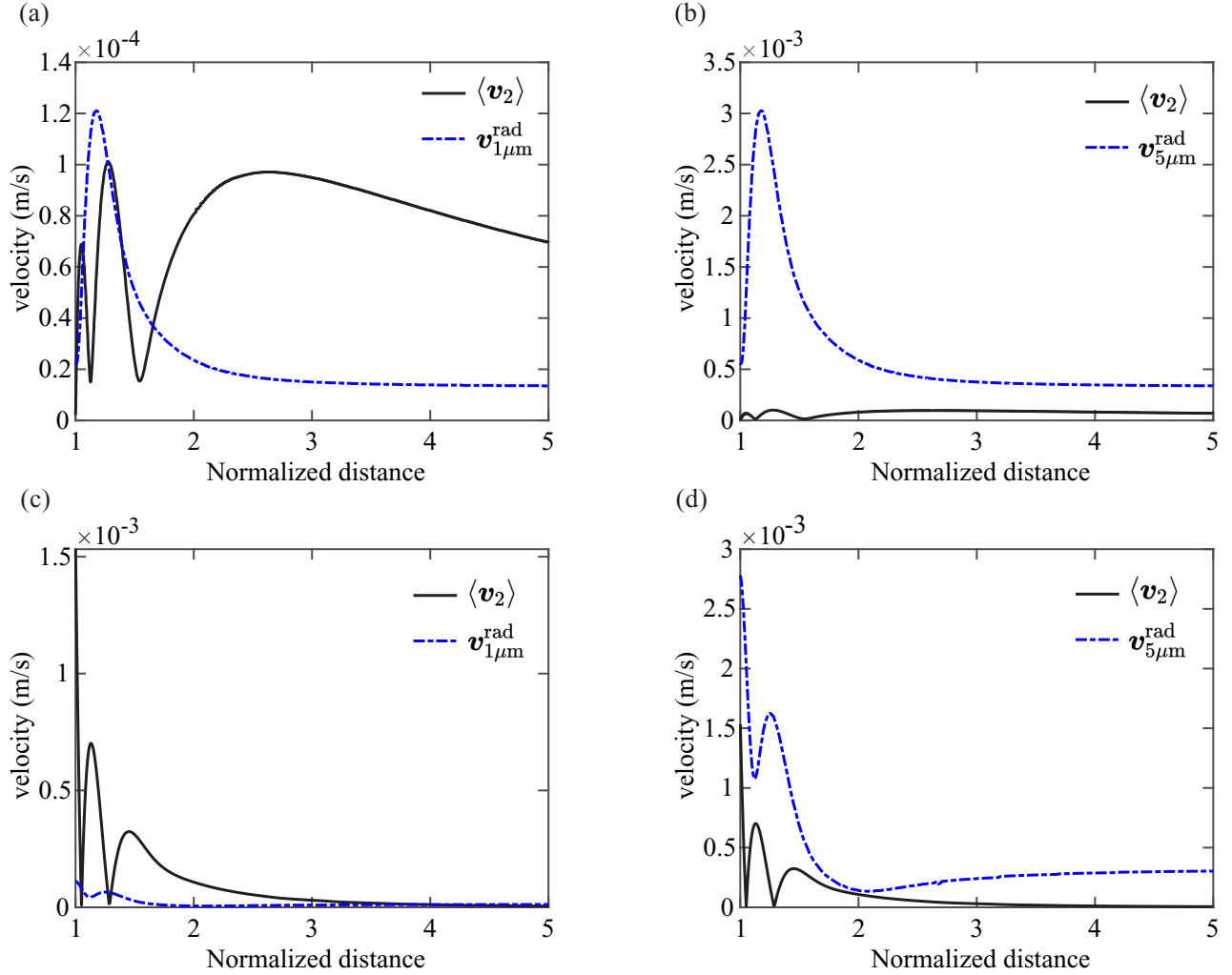


FIG. 11. Directional dependence of critical transition size. (a), (b) The streaming velocity $\langle v_2 \rangle$ and radiation-dominated velocity (v^{rad}) along a radial line segment passing through the center of the scatterer and drawn along the x axis for immersed particles of sizes 1 and 5 μm , respectively. (c), (d) The corresponding velocities along a radial line segment passing through the center of the scatterer and drawn at an angle of 45° with the x axis. The distance is normalized with respect to the scatterer radius.

particles of size 1 μm [Fig. 11(a)] are dominated mainly by the streaming field. In proximity to the scatterer, there are areas where the radiation force contributions are larger than the streaming contributions. However, as the particle size is increased to 5 μm [Fig. 11(b)], the dominance of the radiation force increases and the motion is completely dominated by the radiation force. Figures 11(c) and 11(d) show the corresponding plots for a radial line segment drawn at 45° relative to the x axis. Comparing Figs. 11(a) and 11(c), one can observe a strong directional dependence in the relative dominance of streaming and radiation force. Specifically, in contrast to Fig. 11(a), Fig. 11(c) indicates a more prominent dominance of streaming contributions, even near the scatterer. A similar trend is observed in the comparison of Figs. 11(b) and 11(d), where the radiation force contributions are dominant in both cases, but the relative dominance shows a significant dependence on the direction. These results can be explained by considering the spatial nature of the streaming and radiation force fields, shown in Figs. 3, 6, 8. Specifically, the streaming and radiation force fields vary along both the

radial and angular directions, leading to a spatial variation of their relative contributions to the particle motion. Combined with the analysis presented in Fig. 10, these results illustrate that the critical transition size varies spatially both in the radial and angular directions.

V. CONCLUSION

We investigated the radiation and streaming fields, and the resulting acoustophoresis, around a scatterer by employing a perturbation-approach-based numerical model. We studied various combinations of the acoustic frequency, scatterer material, and the surrounding fluid to elucidate their impact on the acoustophoresis in the vicinity of a scatterer. We also defined and investigated the critical transition size at which the particle motion transitions from being streaming dominated to being radiation dominated.

Our numerical results indicate that the choice of acoustic frequency, scatterer material, and the surrounding fluid significantly impacts the acoustophoresis around the scatterer.

Specifically, for a given scatterer-fluid system, an increase in acoustic frequency leads to an increase in the acoustic radiation force and a decrease in the streaming velocity. Accordingly, the critical transition size for a specific scatterer-fluid system decreases with increasing frequency. In line with this observation, we tracked the motion of 1 and 5 μm particles to illustrate that the motion of particles of a specific size can be dictated by the streaming field, the radiation field, or both, depending on the actuation frequency. In other words, the motion of particles of a specific size can be tuned to be either streaming dominated or radiation dominated by tuning the actuation frequency.

Our results also reveal significant differences in radiation and streaming fields around scatterers with varying contrast factors. The radiation force field for nonrigid scatterers is characterized by the presence of counter-rotating vortices; however, these vortices diminish in size with increasing contrast factor and vanish completely in the limiting case of a perfectly rigid scatterer, resulting in a typical focusing force field. Similarly, the streaming field for nonrigid scatterers is characterized by three pairs of counter-rotating vortices; however, the innermost pair of vortices becomes smaller with increase in contrast factor, and disappears in the limiting case of a perfectly rigid scatterer. Further, the critical transition size decreases with an increase in acoustic contrast factor, with a perfectly rigid scatterer yielding the lowest critical transition size; these results favor the choice of scatterer materials with large acoustic contrast factor for trapping small particles.

Next, we compared the radiation and streaming fields for two different choices of surrounding fluid to assess the impact of fluid properties. Since changing the surrounding fluid for a specific scatterer material changes the acoustic contrast factor, our results reveal a similar trend as observed for the analysis of different scatterer materials for a specific fluid. In addition, our results reveal that a wider range of critical transition size can be achieved for a fluid with higher kinematic viscosity; this observation is in good agreement with prior theoretical analysis by Barnkob *et al.* [51] for acoustophoresis of particles subjected to a purely standing wave field.

Lastly, we performed a spatial analysis of the critical transition size by considering the relative contributions of the streaming and radiation force to the total particle velocity at different locations in the domain. As expected, small and large particles are observed to be dominated by streaming and radiation force, respectively, in most of the regions of the domain. However, the particles with sizes near the transition size may be dominated by streaming or radiation, depending on the spatial location.

Overall, our results reveal that increasing the acoustic contrast factor, lowering the kinematic viscosity of the fluid, and increasing the acoustic frequency offer the most promis-

ing path to realize the manipulation of small particles in scatterer-based acoustofluidic systems. Our results systematically explain the previously reported observations from several experimental reports concerning particle trapping, and clarify the experimental results in relation to the choice of specific scatterer material and acoustic frequency; these choices are seldom justified in experimental reports. Therefore, we believe that the results reported in this article will not only provide a better understanding of acoustophoresis around a scatterer, but will also significantly aid in identifying the optimal design and operational parameters for future experimental studies.

We remark that the immersed microparticles, in general, can experience significant acoustic interaction force that is generated solely due to the presence of other particles in the acoustic field. Recent works have explored the acoustic interaction force between two particles in a standing wave field, while accounting for the microstreaming around the particles [63,64]. Additionally, in the current work, we have considered a two-dimensional setup with a cylindrical scatterer; this corresponds to a very long cylindrical scatterer with a very deep fluid domain and precludes any variations along the vertical direction. In contrast, typical acoustofluidic systems employ microchannels with shallow depth, which introduces a vertical dependence of the acoustic and flow fields in the microchannel due to the no-slip boundary condition at the top and bottom of the microchannel. While three-dimensional simulations can be attempted to study these effects, they often necessitate the use of additional simplifying assumptions to keep computational costs tractable. Moreover, prior 2D simulations of scatterer-based systems have provided good agreement with experimental observations [12,57]. Nonetheless, pending the availability of experimental validation data, the current results should be viewed as instructive. We believe that the next important step in understanding scatterer-based acoustofluidic systems would be to obtain detailed experimental measurements of particle trajectories and critical transition sizes in these systems. Such experimental data will provide important insights into the impact of the presence of channel walls and multiparticle interactions and will facilitate further enhancements of our numerical model.

ACKNOWLEDGMENTS

This work was supported by the National Science Foundation (Grant No. OIA-2229636), the Jane Robertson Layman Fund at the University of Nebraska Foundation (Grant No. 01024460), and the Nebraska Center for Integrated Biomolecular Communication (NIH National Institutes of General Medical Sciences, Grant No. P20 GM113126).

-
- [1] X. Ding, P. Li, S.-C. S. Lin, Z. S. Stratton, N. Nama, F. Guo, D. Slotcavage, X. Mao, J. Shi, F. Costanzo *et al.*, Surface acoustic wave microfluidics, *Lab Chip* **13**, 3626 (2013).
[2] T. Laurell and A. Lenshof, *Microscale Acoustofluidics* (Royal Society of Chemistry, Cambridge, 2014).

- [3] W. Wei, Y. Wang, Z. Wang, and X. Duan, Microscale acoustic streaming for biomedical and bioanalytical applications, *TrAC, Trends Anal. Chem.* **160**, 116958 (2023).
[4] D. Ahmed, C. Y. Chan, S.-C. S. Lin, H. S. Muddana, N. Nama, S. J. Benkovic, and T. J. Huang, Tunable, pulsatile chemical

- gradient generation via acoustically driven oscillating bubbles, *Lab Chip* **13**, 328 (2013).
- [5] P.-H. Huang, Y. Xie, D. Ahmed, J. Rufo, N. Nama, Y. Chen, C. Y. Chan, and T. J. Huang, An acoustofluidic micromixer based on oscillating sidewall sharp-edges, *Lab Chip* **13**, 3847 (2013).
- [6] A. Ozcelik, D. Ahmed, Y. Xie, N. Nama, Z. Qu, A. A. Nawaz, and T. J. Huang, An acoustofluidic micromixer via bubble inception and cavitation from microchannel sidewalls, *Anal. Chem.* **86**, 5083 (2014).
- [7] P.-H. Huang, C. Y. Chan, P. Li, N. Nama, Y. Xie, C.-H. Wei, Y. Chen, D. Ahmed, and T. J. Huang, A spatiotemporally controllable chemical gradient generator via acoustically oscillating sharp-edge structures, *Lab Chip* **15**, 4166 (2015).
- [8] H. Bachman, C. Chen, J. Rufo, S. Zhao, S. Yang, Z. Tian, N. Nama, P.-H. Huang, and T. J. Huang, An acoustofluidic device for efficient mixing over a wide range of flow rates, *Lab Chip* **20**, 1238 (2020).
- [9] P.-H. Huang, L. Ren, N. Nama, S. Li, P. Li, X. Yao, R. A. Cuento, C.-H. Wei, Y. Chen, Y. Xie *et al.*, An acoustofluidic sputum liquefier, *Lab Chip* **15**, 3125 (2015).
- [10] S.-Y. Tang, B. Ayan, N. Nama, Y. Bian, J. P. Lata, X. Guo, and T. J. Huang, On-chip production of size-controllable liquid metal microdroplets using acoustic waves, *Small* **12**, 3861 (2016).
- [11] A. A. Nawaz, Y. Chen, N. Nama, R. H. Nissly, L. Ren, A. Ozcelik, L. Wang, J. P. McCoy, S. J. Levine, and T. J. Huang, Acoustofluidic fluorescence activated cell sorter, *Anal. Chem.* **87**, 12051 (2015).
- [12] I. Leibacher, P. Hahn, and J. Dual, Acoustophoretic cell and particle trapping on microfluidic sharp edges, *Microfluid. Nanofluid.* **19**, 923 (2015).
- [13] C. Dillinger, N. Nama, and D. Ahmed, Ultrasound-activated ciliary bands for microrobotic systems inspired by starfish, *Nat. Commun.* **12**, 6455 (2021).
- [14] J. Durrer, P. Agrawal, A. Ozgul, S. C. Neuhaus, N. Nama, and D. Ahmed, A robot-assisted acoustofluidic end effector, *Nat. Commun.* **13**, 6370 (2022).
- [15] D. Ahmed, A. Ozcelik, N. Bojanala, N. Nama, A. Upadhyay, Y. Chen, W. Hanna-Rose, and T. J. Huang, Rotational manipulation of single cells and organisms using acoustic waves, *Nat. Commun.* **7**, 11085 (2016).
- [16] D. J. Collins, B. Morahan, J. Garcia-Bustos, C. Doerig, M. Plebanski, and A. Neild, Two-dimensional single-cell patterning with one cell per well driven by surface acoustic waves, *Nat. Commun.* **6**, 8686 (2015).
- [17] M. Baudoin and J.-L. Thomas, Acoustic tweezers for particle and fluid micromanipulation, *Annu. Rev. Fluid Mech.* **52**, 205 (2020).
- [18] Y. Chen, X. Ding, S.-C. Steven Lin, S. Yang, P.-H. Huang, N. Nama, Y. Zhao, A. A. Nawaz, F. Guo, W. Wang *et al.*, Tunable nanowire patterning using standing surface acoustic waves, *ACS Nano* **7**, 3306 (2013).
- [19] F. Guo, P. Li, J. B. French, Z. Mao, H. Zhao, S. Li, N. Nama, J. R. Fick, S. J. Benkovic, and T. J. Huang, Controlling cell-cell interactions using surface acoustic waves, *Proc. Natl. Acad. Sci.* **112**, 43 (2015).
- [20] S. Li, X. Ding, Z. Mao, Y. Chen, N. Nama, F. Guo, P. Li, L. Wang, C. E. Cameron, and T. J. Huang, Standing surface acoustic wave (SSAW)-based cell washing, *Lab Chip* **15**, 331 (2015).
- [21] J. Shi, S. Yazdi, S.-C. S. Lin, X. Ding, I.-K. Chiang, K. Sharp, and T. J. Huang, Three-dimensional continuous particle focusing in a microfluidic channel via standing surface acoustic waves (SSAW), *Lab Chip* **11**, 2319 (2011).
- [22] M. Antfolk, P. B. Muller, P. Augustsson, H. Bruus, and T. Laurell, Focusing of sub-micrometer particles and bacteria enabled by two-dimensional acoustophoresis, *Lab Chip* **14**, 2791 (2014).
- [23] M. Kiyasatfar and N. Nama, Particle manipulation via integration of electro-osmotic flow of power-law fluids with standing surface acoustic waves (SSAW), *Wave Motion* **80**, 20 (2018).
- [24] Y. Xie, N. Nama, P. Li, Z. Mao, P.-H. Huang, C. Zhao, F. Costanzo, and T. J. Huang, Probing cell deformability via acoustically actuated bubbles, *Small* **12**, 902 (2016).
- [25] Y. Xie, C. Chindam, N. Nama, S. Yang, M. Lu, Y. Zhao, J. D. Mai, F. Costanzo, and T. J. Huang, Exploring bubble oscillation and mass transfer enhancement in acoustic-assisted liquid-liquid extraction with a microfluidic device, *Sci. Rep.* **5**, 12572 (2015).
- [26] C. Chindam, N. Nama, M. Ian Lapsley, F. Costanzo, and T. Jun Huang, Theory and experiment on resonant frequencies of liquid-air interfaces trapped in microfluidic devices, *J. Appl. Phys.* **114**, 194503 (2013).
- [27] P. B. Muller, R. Barnkob, M. J. H. Jensen, and H. Bruus, A numerical study of microparticle acoustophoresis driven by acoustic radiation forces and streaming-induced drag forces, *Lab Chip* **12**, 4617 (2012).
- [28] A. Ozcelik, N. Nama, P.-H. Huang, M. Kaynak, M. R. McReynolds, W. Hanna-Rose, and T. J. Huang, Acoustofluidic rotational manipulation of cells and organisms using oscillating solid structures, *Small* **12**, 5120 (2016).
- [29] M. Ovchinnikov, J. Zhou, and S. Yalamanchili, Acoustic streaming of a sharp edge, *J. Acoust. Soc. Am.* **136**, 22 (2014).
- [30] T. JunáHuang *et al.*, A reliable and programmable acoustofluidic pump powered by oscillating sharp-edge structures, *Lab Chip* **14**, 4319 (2014).
- [31] C. Tian, W. Liu, R. Zhao, T. Li, J. Xu, S.-W. Chen, and J. Wang, Acoustofluidics-based enzymatic constant determination by rapid and stable in situ mixing, *Sens. Actuators, B* **272**, 494 (2018).
- [32] M. Xu, P. V. Lee, and D. J. Collins, Microfluidic acoustic sawtooth metasurfaces for patterning and separation using traveling surface acoustic waves, *Lab Chip* **22**, 90 (2021).
- [33] A. Pavlic, C. L. Harshbarger, L. Rosenthaler, J. G. Snedeker, and J. Dual, Sharp-edge-based acoustofluidic chip capable of programmable pumping, mixing, cell focusing, and trapping, *Phys. Fluids* **35**, 022006 (2023).
- [34] W. S. Harley, K. Kolesnik, M. Xu, D. E. Heath, and D. J. Collins, 3D acoustofluidics via subwavelength microresonators, *Adv. Funct. Mater.* **33**, 2211422 (2023).
- [35] M. Kaynak, A. Ozcelik, N. Nama, A. Nourhani, P. E. Lammert, V. H. Crespi, and T. J. Huang, Acoustofluidic actuation of *in situ* fabricated microrotors, *Lab Chip* **16**, 3532 (2016).
- [36] N. Nama, P.-H. Huang, T. J. Huang, and F. Costanzo, Investigation of micromixing by acoustically oscillated sharp edges, *Biomicrofluidics* **10**, 024124 (2016).

- [37] P.-H. Huang, C. Y. Chan, P. Li, Y. Wang, N. Nama, H. Bachman, and T. J. Huang, A sharp-edge-based acoustofluidic chemical signal generator, *Lab Chip* **18**, 1411 (2018).
- [38] P.-H. Huang, S. Zhao, H. Bachman, N. Nama, Z. Li, C. Chen, S. Yang, M. Wu, S. P. Zhang, and T. J. Huang, Acoustofluidic synthesis of particulate nanomaterials, *Adv. Sci.* **6**, 1900913 (2019).
- [39] L. Ren, N. Nama, J. M. McNeill, F. Soto, Z. Yan, W. Liu, W. Wang, J. Wang, and T. E. Mallouk, 3D steerable, acoustically powered microswimmers for single-particle manipulation, *Sci. Adv.* **5**, eaax3084 (2019).
- [40] J. M. McNeill, N. Nama, J. M. Braxton, and T. E. Mallouk, Wafer-scale fabrication of micro-to nanoscale bubble swimmers and their fast autonomous propulsion by ultrasound, *ACS Nano* **14**, 7520 (2020).
- [41] N. Nama, R. Barnkob, Z. Mao, C. J. Kähler, F. Costanzo, and T. J. Huang, Numerical study of acoustophoretic motion of particles in a PDMS microchannel driven by surface acoustic waves, *Lab Chip* **15**, 2700 (2015).
- [42] N. Nama, T. J. Huang, and F. Costanzo, Acoustic streaming: An arbitrary Lagrangian-Eulerian perspective, *J. Fluid Mech.* **825**, 600 (2017).
- [43] R. Barnkob, N. Nama, L. Ren, T. J. Huang, F. Costanzo, and C. J. Kähler, Acoustically driven fluid and particle motion in confined and leaky systems, *Phys. Rev. Appl.* **9**, 014027 (2018).
- [44] T. Baasch, A. Pavlic, and J. Dual, Acoustic radiation force acting on a heavy particle in a standing wave can be dominated by the acoustic microstreaming, *Phys. Rev. E* **100**, 061102(R) (2019).
- [45] W. L. Nyborg, Acoustic streaming near a boundary, *J. Acoust. Soc. Am.* **30**, 329 (1958).
- [46] C. Chen, S. P. Zhang, Z. Mao, N. Nama, Y. Gu, P.-H. Huang, Y. Jing, X. Guo, F. Costanzo, and T. J. Huang, Three-dimensional numerical simulation and experimental investigation of boundary-driven streaming in surface acoustic wave microfluidics, *Lab Chip* **18**, 3645 (2018).
- [47] H. Bruus, Acoustofluidics 7: The acoustic radiation force on small particles, *Lab Chip* **12**, 1014 (2012).
- [48] M. Settles and H. Bruus, Forces acting on a small particle in an acoustical field in a viscous fluid, *Phys. Rev. E* **85**, 016327 (2012).
- [49] A. Pavlic, P. Nagpure, L. Ermanni, and J. Dual, Influence of particle shape and material on the acoustic radiation force and microstreaming in a standing wave, *Phys. Rev. E* **106**, 015105 (2022).
- [50] M. Koklu, A. C. Sabuncu, and A. Beskok, Acoustophoresis in shallow microchannels, *J. Colloid Interface Sci.* **351**, 407 (2010).
- [51] R. Barnkob, P. Augustsson, T. Laurell, and H. Bruus, Acoustic radiation-and streaming-induced microparticle velocities determined by microparticle image velocimetry in an ultrasound symmetry plane, *Phys. Rev. E* **86**, 056307 (2012).
- [52] A. R. Selfridge, Approximate material properties in isotropic materials, *IEEE Trans. Sonics Ultrason.* **32**, 381 (1985).
- [53] L. D. Landau, E. M. Lifshits, and A. M. Kosevich, *Theory of Elasticity*, 3rd ed., Course of Theoretical Physics, Vol. 7 (Pergamon Press, 1986), p. 187.
- [54] J. Rumble, *CRC Handbook of Chemistry and Physics* (CRC Press, Boca Raton, FL, 2018).
- [55] M. Holmes, N. Parker, and M. Povey, Temperature dependence of bulk viscosity in water using acoustic spectroscopy, *J. Phys.: Conf. Ser.* **269**, 012011 (2011).
- [56] Z. Chen, P. Liu, X. Zhao, L. Huang, Y. Xiao, Y. Zhang, J. Zhang, and N. Hao, Sharp-edge acoustic microfluidics: Principles, structures, and applications, *Appl. Mater. Today* **25**, 101239 (2021).
- [57] N. Nama, P.-H. Huang, T. J. Huang, and F. Costanzo, Investigation of acoustic streaming patterns around oscillating sharp edges, *Lab Chip* **14**, 2824 (2014).
- [58] COMSOL Multiphysics v. 6.0, COMSOL AB, Stockholm, Sweden, 2020.
- [59] A. A. Doinikov, M. S. Gerlt, A. Pavlic, and J. Dual, Acoustic streaming produced by sharp-edge structures in microfluidic devices, *Microfluid. Nanofluid.* **24**, 32 (2020).
- [60] A. A. Doinikov, M. S. Gerlt, and J. Dual, Acoustic radiation forces produced by sharp-edge structures in microfluidic systems, *Phys. Rev. Lett.* **124**, 154501 (2020).
- [61] See Supplemental Material at <http://link.aps.org/supplemental/10.1103/PhysRevE.108.045102> for further results on mesh convergence.
- [62] J. Hu, L. Ong, C. Yeo, and Y. Liu, Trapping, transportation and separation of small particles by an acoustic needle, *Sens. Actuators, A* **138**, 187 (2007).
- [63] A. Pavlic, L. Ermanni, and J. Dual, Interparticle attraction along the direction of the pressure gradient in an acoustic standing wave, *Phys. Rev. E* **105**, L053101 (2022).
- [64] S. Sepehrirahnama, A. R. Mohapatra, S. Oberst, Y. K. Chiang, D. A. Powell, and K.-M. Lim, Acoustofluidics 24: Theory and experimental measurements of acoustic interaction force, *Lab Chip* **22**, 3290 (2022).